nature chemistry

Fast galvanic lithium corrosion involving a Kirkendall-type mechanism

Dingchang Lin [1,3], Yayuan Liu [1,3], Yanbin Li[1], Yuzhang Li[1], Allen Pei [1], Jin Xie[1], William Huang [1] and Yi Cui [1,2]*

Developing a viable metallic lithium anode is a prerequisite for next-generation batteries. However, the low redox potential of lithium metal renders it prone to corrosion, which must be thoroughly understood for it to be used in practical energy-storage devices. Here we report a previously overlooked mechanism by which lithium deposits can corrode on a copper surface. Voids are observed in the corroded deposits and a Kirkendall-type mechanism is validated through electrochemical analysis. Although it is a long-held view that lithium corrosion in electrolytes involves direct charge-transfer through the lithium–electrolyte interphase, the corrosion observed here is found to be governed by a galvanic process between lithium and the copper substrate—a pathway largely neglected by previous battery corrosion studies. The observations are further rationalized by detailed analyses of the solid–electrolyte interphase formed on copper and lithium, where the disparities in electrolyte reduction kinetics on the two surfaces can account for the fast galvanic process.

C orrosion is a chemical degradation process commonly observed when materials are exposed to environments with a high redox power[1]. Electrochemical cells, which involve highly oxidative and reductive redox pairs in ion-concentrated environments, usually encounter corrosion to various extents[2,3]. Therefore, in most of the practical electrochemical systems, the redox pairs are carefully chosen to fall into (or not far beyond) the thermodynamic stability window of the electrolytes in order to circumvent corrosion. The rechargeable lithium ion battery (LIB), however, is a rather special system in which the potential of the electrodes often falls far beyond the stability limit of the electrolyte to maximize the energy density[4,5]. As a result, unlike a thermodynamically stable system, corrosion can easily occur in LIBs unless an effective kinetic inhibition is applied, and such corrosion has drawn the attention of the battery community[6]. Fortunately for conventional lithium ion chemistries, satisfactory combinations of redox pairs and electrolytes capable of forming a dense passivating solid–electrolyte interphase (SEI) were found[4,5,7]. They were proved to be relatively stable within the battery service life, which has made LIBs a successful means of energy storage over the past two decades.

Nowadays, the burgeoning developments of renewable energy, portable electronics and electric vehicles are demanding electrochemical energy storage devices with an even higher energy density[5,8]. Metallic Li-based chemistries, such as lithium–sulfur and lithium–oxygen, have the potential to replace LIBs[9] thanks to the over tenfold higher theoretical capacity of Li (3,860 mAh g^{-1}, compared to the 372 mAh g^{-1} of conventional graphite). Therefore, studies of metallic Li, including its fundamental properties[10–13], electrolyte chemistries[14–16], interfacial engineering[17–19] and electrode designs[20,21], have been conducted intensively in recent years. However, metallic Li is highly susceptible to corrosion due to its low redox potential ($E^0_{(Li^+/Li^0)} = -3.04$ V versus the standard hydrogen electrode)[13,20–25], which is one of the dominant factors that dictates its cycling stability. Although the SEI concept that resulted from Li corrosion studies has been well established[26–32], a systematic understanding of the corrosion process beyond the initial SEI formation

stage remains elusive. A long-held view is that Li can be passivated by the SEI that forms rapidly in the liquid electrolyte, after which corrosion is eliminated by the blockage of electron transfer[29,32–34]. However, if such an assumption is untrue or additional corrosion pathways exist, the limited electrolyte and Li in the cells would be consumed continuously and so cause capacity fading. Moreover, previous studies on the Li metal anode mostly employed continuous cycling conditions, which is very rare in practice. In reality, cycling protocols are far more complicated, as they involve rests and recurring charge/discharge at different states of charge[35]. Therefore, it is critical to study Li corrosion in long-term rest and more practical scenarios.

Here we observe the fast corrosion of Li on a heterogeneous conductive surface and provide insights into the mechanism at play. The study represents well the real circumstances in Li metal batteries, where Li deposition/dissolution occur on a copper current collector. We found that the corrosion of Li on Cu can be described by the typical Kirkendall effect[36], a phenomenon that attributes void formation to the disparities between inward and outward mass transport (the synthesis of hollow metal oxides via the oxidation of metal nanocrystals is an interesting example of the nanoscale Kirkendall effect[37,38]). The observed fast Kirkendall-type corrosion also tends to induce dendritic growth during subsequent plating. The fast corrosion of Li is found to involve a galvanic process[39], whereby Li and the more noble Cu serve as the anode and the cathode, respectively. The galvanic corrosion mechanism is further elucidated by the structural and compositional analyses of the SEI on Cu and Li. Our findings reveal an additional failure mechanism of Li metal anodes, and shed light on their long-term stability in storage and under non-ideal operation conditions. Through this report, we hope to raise awareness in the battery community of the corrosion issues and mechanisms.

Results and discussions

Morphological evolution of corroded Li deposits. To characterize the corrosion process, Li was deposited on clean Cu at a current

[1]Department of Materials Science and Engineering, Stanford University, Stanford, CA, USA. [2]Stanford Institute for Materials and Energy Sciences, SLAC National Accelerator Laboratory, Menlo Park, CA, USA. [3]These authors contributed equally: Dingchang Lin, Yayuan Liu. *e-mail: yicui@stanford.edu

density of $0.5\,mA\,cm^{-2}$ and a total charge of $0.18\,C\,cm^{-2}$ $(0.05\,mAh\,cm^{-2})$. The liquid electrolyte employed, without further specification, was $1.0\,M$ lithium bis(trifluoromethane)sulfonimide (LiTFSI) in 1:1 w/w 1,3-dioxolane (DOL)/1,2-dimethoxyethane with 2 wt% $LiNO_3$, which is a prototypic electrolyte for lithium–sulfur and lithium–oxygen chemistries. The addition of $LiNO_3$ afforded spherical Li deposits with a relatively uniform size (Supplementary Fig. 1), rather than the mossy or dendritic counterparts[10,40], which is beneficial for quantitative analyses. Prior to deposition, the Cu was held potentiostatically at 0 V versus Li^+/Li^0 for ~12 hours to preform the SEI. Once the SEI on Cu was stabilized, Li nucleated underneath the SEI and deposited locally, whereas regions without deposition were still protected by the preformed SEI (Supplementary Figs. 2 and 3). Otherwise, Li was consumed rapidly to stabilize the SEI across the electrode within a few hours of deposition (Supplementary Fig. 4), which prevented the observation of the chronic corrosion process that is the focus of our study.

The morphological evolution of Li deposits was visualized by scanning electron microscopy (SEM) with focused-ion-beam (FIB) milling (Fig. 1a–c) and by cryogenic electron microscopy (cryo-EM) (Fig. 1d–f). Various durations of rest in the electrolyte were applied prior to imaging (0–200 hours). The as-deposited Li was observed to be spherical with a solid core (Fig. 1a). As seen from Supplementary Movie 1, no voids were observed in the majority of the as-deposited Li particles, but a small proportion of them exhibited slightly concave surfaces (particles 5 and 9) owing to the concurrent corrosion at deposition. The solid nature of the as-deposited Li was further confirmed by cryo-EM (Fig. 1d), a recently developed technique to visualize sensitive battery materials in a high-resolution and non-destructive fashion[41]. The imaged Li shows a light contrast, which indicates no compositional conversion of the low-atomic-number Li under the cryogenic conditions or during the specimen transfer.

When the Li deposits were rested in electrolyte for 100 hours, discernible internal voids could be visualized after FIB milling (Fig. 1b, voids marked with red dash lines). The void fraction of the corroded particles (Supplementary Movie 2) were semiquantitatively resolved by image segmentation, and afforded a value of ~45.6% with a standard deviation of 15.0. In addition to the voiding, pronounced surface concavities were also observed on most of the deposits, which can be ascribed to the collapse of the flexible SEI after Li loss (Supplementary Fig. 5). The cryo-EM image (Fig. 1e) coincided with the FIB/SEM results, in which Li deposits also exhibited obvious voids (marked with red dash lines). After 200 hours of rest in the electrolyte, as illustrated in Fig. 1c, almost all the deposited Li was lost to leave near-empty SEI shells. Many of the remaining SEI shells were highly crumpled, as clearly shown in the cryo-EM image (Fig. 1f).

From the above information, we can construct three-dimensional (3D) models to illustrate the morphological evolution of Li deposits when rested in the electrolyte, which resembles the typical Kirkendall effect (Fig. 1g–i). Starting from freshly deposited spherical Li (Fig. 1g), corrosion occurred gradually with the formation of enlarging voids and concave SEI. After ~100 hours, the voids and concavities became highly discernible (Fig. 1h) with an approximately 50% Li loss. And almost all the Li succumbed to side reactions after ~200 hours to leave concave or crumpled SEI shells on the Cu (Fig. 1i).

The morphological evolution of Li was also studied at higher deposition currents (Supplementary Figs. 6 and 7) and similar results obtained. The corrosion was even more pronounced in smaller deposits (~200 nm), where a distinct yolk–shell structure appeared after only four hours of rest (Supplementary Fig. 8). Comparable corrosion behaviour was also observed in other electrolytes, including carbonate (Supplementary Fig. 9).

According to the conventional understanding, Li in an electrolyte should undergo a relatively short SEI formation stage, in which
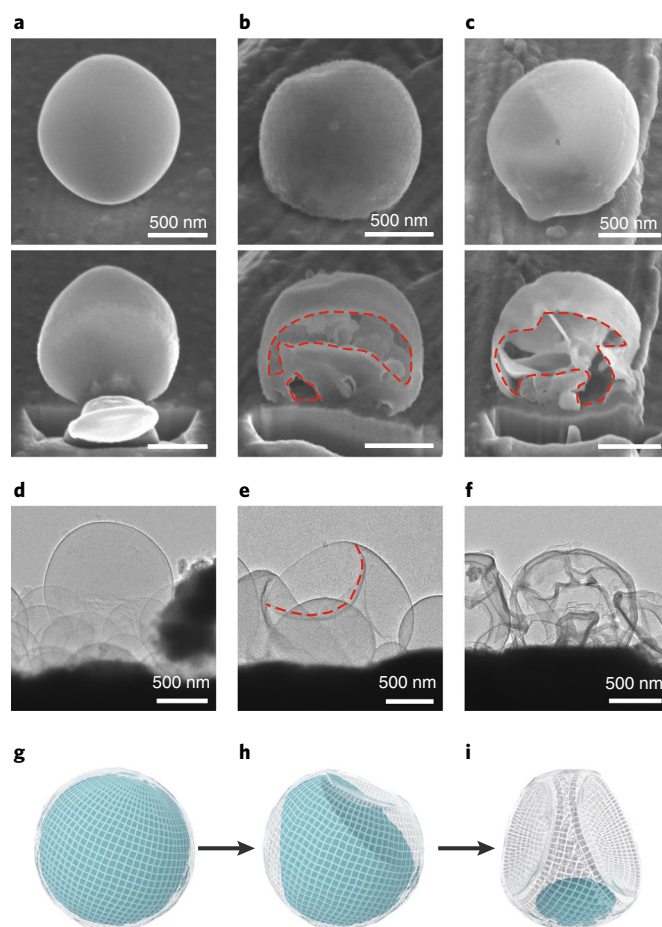

Fig. 1 | Kirkendall voids formed in Li deposits. a–c, SEM images of Li deposits $(0.18\,C\,cm^{-2})$ on Cu substrates after 0 (**a**), 100 (**b**) and 200 (**c**) hours of rest in the liquid electrolyte. The top images show the uncut Li particles and the bottom ones show the same particles cut by FIB. **d–f**, Cryo-EM images of Li deposits on Cu after 0 (**d**), 100 (**e**) and 200 (**f**) hours of rest in the liquid electrolyte. The Cu substrates were held at 0 V versus Li^+/Li^0 for ~12 h to preform a protective SEI on Cu. A current density of $0.5\,mA\,cm^{-2}$ was applied for the deposition. The contours of the voids are highlighted with red dashed lines. **g–i**, 3D models of the Li deposits on Cu after 0 (**g**), 100 (**h**) and 200 (**i**) hours of rest in the liquid electrolyte. The transparent shells indicate that the SEI films formed on the outer surface of Li (blue). Latitude and longitude lines are shown on the SEI shells to better illustrate the surface curvatures.

the SEI could gradually stabilize and ultimately prevent further corrosion by blocking the electron transfer[29,32–34]. However, we did not observe the expected termination of Li corrosion even after a prolonged rest of hundreds of hours. This implies the existence of additional corrosion pathways in the battery, which we discuss in later sections.

Besides losing active material, Li corrosion may induce other severe side effects. For example, we observed an altered deposition behaviour in the presence of corroded Li. In the study, Li was first deposited galvanostatically, followed by an interval rest of five hours before the second deposition. It was found that during the second deposition, dendritic Li was more likely to grow from the corroded regions (Fig. 2a). We further performed protocols that involved multiple depositions with interval rests. In the case of four depositions with three interval rests, the repeated growth of spherical/dendritic Li initiated from a single nucleus was observed (Supplementary Fig. 10c,d), and dendritic Li preferentially evolved
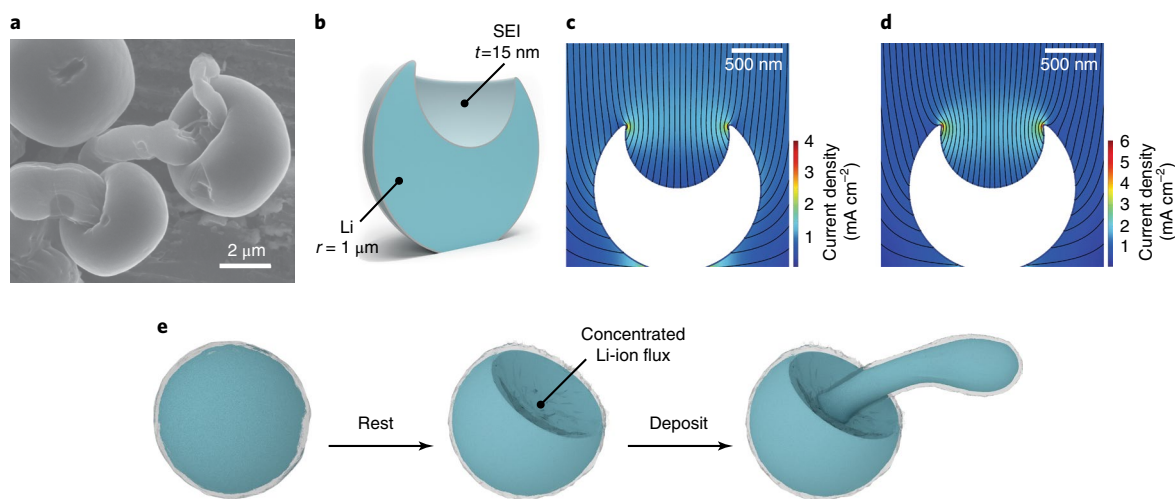
Fig. 2 | Dendritic Li growth on Li deposits with interval rests. a, SEM image of Li deposits after two successive depositions with an interval rest of 5 h (0.36 C cm^{-2} for each deposition). Li grows in dendritic form from the concave surfaces of the corroded Li at the second deposition. **b**, The hemisected 3D model illustrates the morphology of the corroded Li used for the simulation of the Li ion flux, where the radius of Li (r) was set to 1 μm and the thickness of the SEI (t) was defined as 15 nm. A full 3D particle was used for the finite element analysis calculation. **c**, Calculated distribution of the Li ion flux near the corroded Li deposit, where the Li ion diffusion coefficient is identical across the whole Li surface SEI. **d**, Simulated distribution of the Li ion flux near the corroded Li deposit when the Li ion diffusion coefficient of the SEI on the concave surface is tenfold higher than that on the other surfaces. **e**, 3D illustration of the dendritic Li that grows from the concave surface of a corroded Li particle when an interval rest is applied between two depositions.

from the corroded concave spots. However, if Li was deposited continuously, spherical shapes could still be maintained even at larger deposition capacities (1.8–3.6 C cm^{-2}, Supplementary Fig. 11). To elucidate the mechanism behind the altered deposition morphology, the ionic flux across the corroded Li particles was simulated using finite element analysis, based on a 3D Li deposit model with a radius of 1 μm, a concave surface radius of 0.6 μm and a SEI thickness of 15 nm (Fig. 2b). Even if the ion transport characteristics are assumed identical across the whole Li surface (Fig. 2c and Supplementary Fig. 12), the Li ion flux can be concentrated at the concave region by a geometric effect[25]. In practice, concave SEI can potentially experience stress and become defective, which causes an increase in Li ion diffusivity. When a tenfold-higher Li ion diffusion coefficient was imposed over the concave surface, an even more concentrated Li ion flux could be resolved (Fig. 2d). Further increasing the diffusion coefficient at the concavities had a minimal effect on the ionic flux distribution (Supplementary Fig. 12). Therefore, we conclude that both the geometric effect and the change in local Li ion diffusivity facilitated the preferential Li nucleation inside the corroded pits during successive depositions (Fig. 2e)[42].

Quantitative analysis of corrosion kinetics. The Li corrosion rate on Cu was further quantified via a time-dependent Coulombic loss study, in which the Coulombic efficiency was defined as the ratio of the dissolution capacity to the initial deposition capacity (Fig. 3). Note that 'dead' Li formation, commonly observed in carbonate electrolytes[43], was rare in the ether electrolyte and cycling conditions employed here, as the low-aspect-ratio Li is less likely to be electrically disconnected from the substrate during dissolution (Supplementary Fig. 13). Therefore, the Coulombic loss here can be confidently attributed to Li corrosion.

The black dots in Fig. 3 present the Coulombic efficiency evolution on Cu with the SEI preformed via a potentiostatic process aligned with the condition in Fig. 1 and the blue and red dots show the trend when the SEI was preformed galvanostatically at a relatively high (0.5 mA cm^{-2}, as for the condition in Supplementary Fig. 4) and low (0.02 mA cm^{-2}) current, respectively. The typical voltage profiles of the tests are shown in Supplementary Figs. 14–16. Among the three
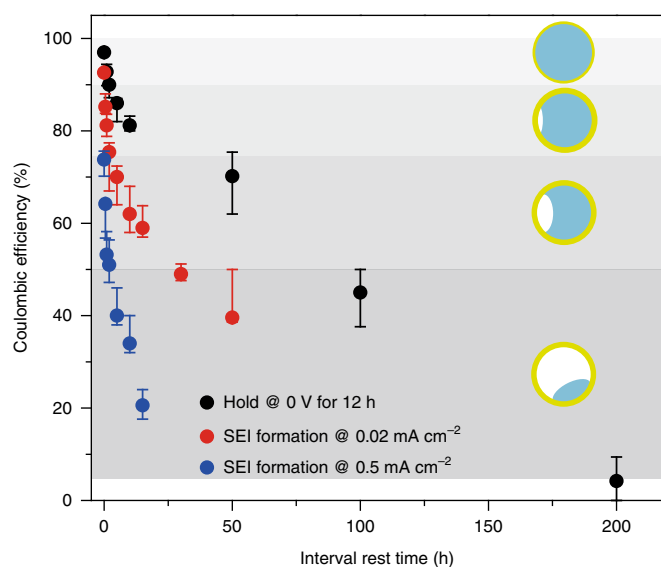

Fig. 3 | Coulombic loss of Li at various rest times. The coulombic efficiency of Li deposited on Cu after various rest intervals between deposition and dissolution. Black dots show the trend of Coulombic loss with Cu held at 0 V versus Li$^+$/Li^0 for ~12 h before deposition to preform SEI films on Cu. Red and blue dots represent the trends when the SEI formation was performed via the galvanostatic discharging of Cu to 0 V versus Li$^+$/Li^0 at 0.02 and 0.5 mA cm^{-2}, respectively. A current density of 0.5 mA cm^{-2} was employed for both the deposition and dissolution processes. The cutoff voltage for Li dissolution was set at 1 V versus Li$^+$/Li^0. The morphologies of the Li deposits at different Coulombic efficiency ranges (grey shades) are schematically illustrated on the right, where green and blue represent the SEI films and Li, respectively. The data points are from the medians, whereas the upper and lower limits of the error bars are the highest and lowest values in the parallel experiments, respectively.

conditions, Cu with the SEI preformed potentiostatically showed the slowest corrosion (Coulombic efficiency ~45% at 100 hours and ~5% at 200 hours). This coincides with the FIB/SEM and cryo-EM
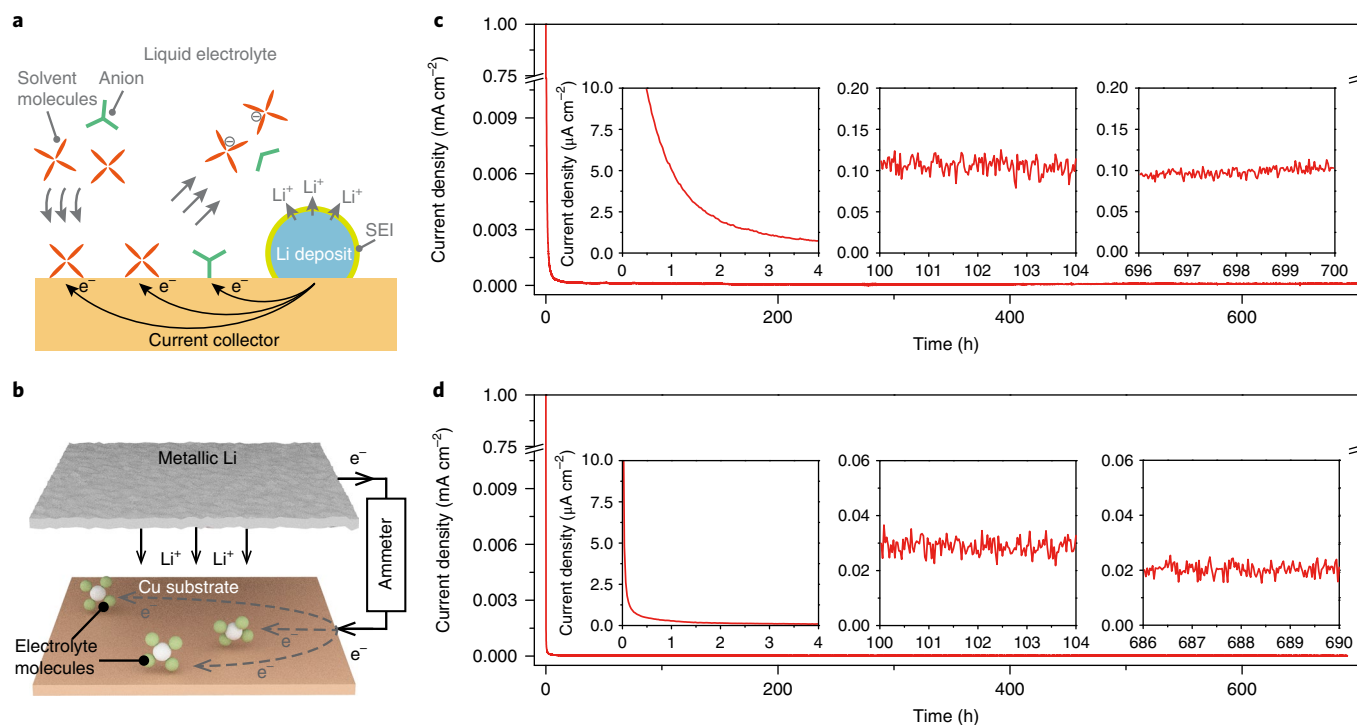
Fig. 4 | Quantifying the galvanic corrosion and proposed mechanisms. a, The proposed mechanisms of galvanic corrosion and the formation of Kirkendall voids. **b**, The schematic shows the galvanic cell for quantifying the corrosion rate of Li through the galvanic processes. Cu and Li foil are the separated cathode and anode, respectively. Cu was held at the same potential as the Li foil while the passed current was recorded. The current represents the galvanic corrosion rate of Li connected to Cu. **c,d**, The current density versus time curves show the galvanic corrosion rate of Li through pristine Cu (**c**) and LiF-coated Cu substrates (**d**). The LiF-protected Cu substrate exhibited a highly reduced galvanic current.

studies, in which ~45.6% of the Li was consumed after resting for 100 hours, and almost all the Li vanished after 200 hours. Moreover, a nearly constant Coulombic loss rate was observed during the later periods of the rest (from ~20 to 200 hours), which indicates that the corrosion may have approached a steady state. When the SEI was preformed at a high current of $0.5\,mA\,cm^{-2}$, virtually no stable SEI was formed on Cu. Therefore, Li corroded in a much faster fashion, with ~50% Li loss after merely 5 hours, which agrees well with the FIB/SEM studies (Supplementary Fig. 4). If the SEI preformation current was reduced to $0.02\,mA\,cm^{-2}$, an apparently more protective SEI was formed on Cu, which afforded a slower corrosion with ~50% Li loss after 30 hours of rest. A galvanic cycling protocol for SEI preformation can also offer a decent Cu stabilization, but it is still inferior to the potentiostatic process (Supplementary Fig. 17). In addition, the corrosion rate can be altered by temperature, and was at least doubled at 60 °C compared to that at room temperature (Supplementary Fig. 18). The Coulombic efficiency evolution study further validates the fast corrosion of Li deposits on Cu, in agreement with our imaging studies.

Li corrosion through galvanic process. Empirically, Li corrosion occurs through a direct charge transfer with the electrolyte species (solvents, anions and so on)[26,42]. Based on the hypothesis, the frontier of the side reactions is proposed to be at the SEI/electrolyte interface rather than the Li/SEI interface, because the compact SEI shell fully blocks the diffusion of solvents and anions[42]. The thickness of the SEI is therefore determined by the tunnelling length of the electrons, beyond which the corrosion would be terminated[44]. However, such a theory cannot account for the continuous, fast corrosion of Li on the Cu surface observed in this study. Correspondingly, we suggest an alternative corrosion pathway that has been almost overlooked, which is the galvanic corrosion of Li in conjunction with

the more noble Cu substrate through an internally formed galvanic cell. In the galvanic cell, Cu and Li serve as the cathode and anode, respectively. Due to the relatively weak passivation power of the SEI on Cu, electrons are transferred from Li to the electrolyte through Cu, with Li+ diffusing outward through the SEI on the Li surface (Fig. 4a). In such a scenario, the dominant outward Li+ diffusion can account well for the observed Kirkendall-type void formation[45].

The corrosion rate extracted from Coulombic loss includes all the possible mechanisms. To quantify the specific contribution from the galvanic process, a galvanic cell was designed in which separated electrodes of Cu and Li in the electrolyte were connected externally through an ammeter, as schematically illustrated in Fig. 4b. The Cu electrode was fixed at 0 V versus Li+/Li0 as the current that passed through the external circuit was recorded over time. The device mimics the pure galvanic corrosion of Li in direct contact with Cu—the measured current indicates the galvanic corrosion rate. Figure 4c shows the time-dependent corrosion current, which was high initially (partially due to the capacitive contribution) and dropped quickly to the $\mu A\,cm^{-2}$ level. Nevertheless, rather than eventually dropping to zero, the galvanic current approached a relatively fixed value (~$0.1\,\mu A\,cm^{-2}$) even after hundreds of hours, which indicates the incessant nature of galvanic corrosion. A similar effect was also observed in a carbonate electrolyte with a slightly slower galvanic corrosion (Supplementary Fig. 19), which can be attributed to the change in SEI composition on Cu. Moreover, as the junction type also affects the galvanic corrosion rate, a faster corrosion might be expected when metals are in direct contact rather than connected by an external circuit[38]. Thus, the real galvanic corrosion rate of Li deposits on Cu could be even higher than the measured value.

By integrating the galvanic corrosion current over time and comparing it with the Coulombic efficiency analyses, the galvanic process turns out to account for ~80% of the total corrosion (a detailed
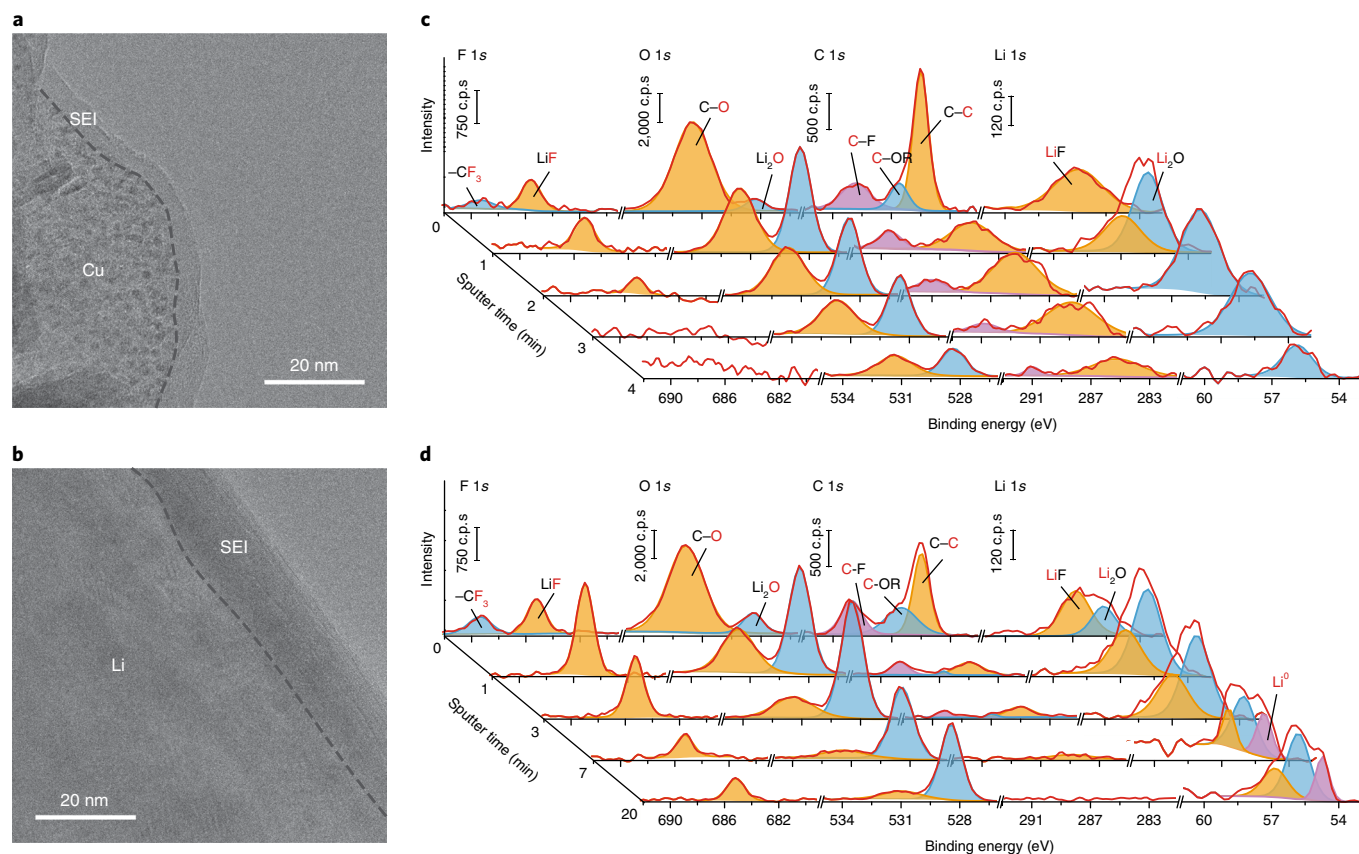
Fig. 5 | SEI analyses on Cu and Li surfaces with cryo-EM and XPS. a, Cryo-EM image of the SEI grown on a Cu surface after fixing the potential of Cu at 0 V versus Li$^+$/Li^0 for 25 h. **b**, Cryo-EM image of the SEI grown on Li after resting in electrolyte for 25 h. The substrate/SEI boundaries are marked with black dashed lines in **a** and **b**. **c**, XPS spectra at various depths of the SEI on the Cu surface after being held at 0 V versus Li$^+$/Li^0 for 25 h. **d**, XPS spectra at various depths of the SEI on Li after being rested in electrolyte for 25 h. c.p.s., counts per second.

calculation is given in Supplementary Methods). The remaining ~20% of the corrosion might come from a direct charge transfer and pitting corrosion on the Li surface. The surface area of Li deposits, nevertheless, was comparable to that of Cu (detailed calculation given in Supplementary Methods), which indicates a much faster corrosion rate (per area) via the galvanic pathway. The result somehow contradicts conventional wisdom, in which compositionally and morphologically similar SEIs, and thus comparable corrosion rates are expected on Cu and Li surfaces for their equipotential nature. In fact, distinct differences in the SEI can be observed on Cu and Li metal surfaces, which is explained in detail in a later section.

The galvanic corrosion can be mitigated by protecting the Cu surface. Here we demonstrated a ~30 nm conformal LiF coating on Cu (LiF@Cu) by atomic layer deposition (ALD) for effective Li anticorrosion (Supplementary Figs. 20 and 21)[17–19]. LiF was chosen for its absolute stability at the Li$^+$/Li^0 potential, negligible solubility in electrolyte and poor electrical conductivity. With a LiF coating, the stabilized galvanic current was ~20 nA cm^{-2} (Fig. 4d). Although still non-zero, the value was only one-fifth of that without LiF (~0.1 μA cm^{-2}). The minute current leakage might be due to cracks, defects and grain boundaries of the LiF, which increase the local electrolyte permeability and ion transport. As a result, compared to pristine Cu, the Coulombic loss of Li deposited on LiF@Cu was drastically slowed down, with a ~70% capacity retention after 200 hours of rest (Supplementary Fig. 23). Note that when Li was deposited onto LiF@Cu, a higher polarization was observed due to the reduced electrical and ionic conductivity (Supplementary Fig. 24). The corresponding Li deposits exhibit near-spherical shapes with faceted features (Supplementary Fig. 25), whereas the

other regions without Li can still be protected by the conformal LiF film (Supplementary Figs. 2 and 3).

The mechanisms behind disparities in corrosion kinetics. To understand the drastic differences in the corrosion rate on Li metal and Cu surfaces, detailed analyses of the SEI on both surfaces were conducted by cryo-EM and X-ray photoelectron spectroscopy (XPS). Cyclic voltammetry shows the electrolyte decomposition potentials (Supplementary Fig. 26; LiNO$_3$ and solvent/LiTFSI reduction can be identified at ~1.7 V and 0–1 V versus Li$^+$/Li^0, respectively), and the possible decomposition products are summarized in Supplementary Fig. 27[10].

Cryo-EM reveals that the thickness of the SEI on Cu is ~5–8 nm (Fig. 5a), which is 2–3 times thinner than that on Li (~15 nm (Fig. 5b)). More importantly, the SEI on Li has a significantly higher degree of crystallinity (Supplementary Figs. 28 and 29) and exhibits a bilayered structure with a dense Li$_2$O shell (the ~0.268 nm lattice spacing can be assigned to the {110} planes of Li$_2$O). Elemental mapping (Supplementary Fig. 30) and electron energy loss spectroscopy (Supplementary Fig. 31) confirmed the presence of oxygen, nitrogen and carbon elements in the SEI. The crystalline domains might impart a greater stability to the SEI on the Li surface.

The composition of the SEIs at various formation times (from 3 to 100 hours) was further studied using XPS depth profiles (Fig. 5c,d and Supplementary Figs. 32–38). Overall, the SEIs on Cu and Li share similar compositions, including inorganics (LiF, Li$_2$O, Li$_x$NO$_y$ and so on) and organics (ROLi, oligomers, polymers and so on), which is not surprising because the two surfaces are thermodynamically equivalent (equipotential). In the early stage

(~3 hours) of SEI formation, both SEIs were rich in organics, but they gradually transformed to being inorganic rich and became stabilized. Nevertheless, drastic differences in SEI thickness, relative ratios of species and their distributions were observed. Consistent with the cryo-EM study, the SEI on Li is much thicker (~2–4 times) than that on Cu. For the SEI on Cu, the Cu $2p$ signals started to appear after ~2–3 minutes of sputtering, which indicates SEI depletion by sputtering; however, for that on Li, the Li^0 $1s$ signals were not observed until 7 or even 20 minutes of sputtering at the same sputtering power. The thickness of both SEIs, surprisingly, barely changed after 3 hours of formation, a finding further supported by SEM (Supplementary Fig. 39) and cryo-EM (Supplementary Fig. 40). Moreover, the SEI on Cu was richer in organics, which are distributed across the whole thickness of the SEI, as indicated by the C $1s$ signals of the XPS spectra. In contrast, the SEI on Li possessed more inorganics (mainly LiF and Li_2O from F $1s$, O $1s$ and Li $1s$ spectra), and the organics and inorganics have a distinct separation.

The differences in SEI can be attributed to the slower reduction kinetics on Cu than on Li, although they share the same thermodynamic driving force (equipotential). It is known that the decomposition of electrolyte is a complex, multielectron and multistep process[10,28,42,46,47], and some reduction reactions, especially the rate-determining steps (which might involve valence bond breaking or the formation of products with a lower oxidation state), can be more favourable with a synergy between charge transfer and nucleo/electrophilic attack. The Li surface exhibits a higher electron density to facilitate the reactions. And such a direct charge transfer would result in a higher Li ion concentration near the Li metal surface, which is also beneficial for the precipitation of inorganics.

With the above discussion, we can now propose a comprehensive mechanism that governs the galvanic corrosion of Li. Due to the fast formation of a thick, inorganic-rich passivation layer on the Li metal surface, both electron tunnelling and solvent/anion diffusion through the SEI can be terminated after a brief period of rest inside the electrolyte, which prevents further corrosion through direct charge transfer[42,48]. However, the electrolyte decomposition on Cu is rather slow and so is unable to afford a compact passivation and might allow continuous mass/charge transport through the interphase. Furthermore, given the much slower reduction kinetics, the reduction products are more likely to stay at higher oxidation states. Rather than precipitating as part of the SEI, these (organic) products are prone to dissolving into the electrolyte[49], which brings about the porous nature of the SEI. In the end, an equilibrium between reduction and dissolution can be reached on the Cu surface, which explains the constant SEI thickness over time in spite of the steady galvanic corrosion.

Galvanic corrosion poses additional challenges on the Li anode, and careful evaluation of the chronic electrode stability is needed in future studies. The possibility for the conductive substrate to be exposed to electrolyte during battery operation should also be minimized. Moreover, the effect should be considered when designing new electrode architectures that involve larger conductive surfaces[20,21]. Several strategies might be employed to mitigate galvanic corrosion. First, current collector passivation with a good electrical insulation and low electrolyte permeability could be developed, and this has emerged as an intensively studied topic for homogenizing Li deposition[17–19]. Second, a planar and dense Li deposition, if it can be fulfilled, will physically isolate the substrate from the electrolyte and block the galvanic corrosion pathway. Third, the development of all-solid-state batteries can help circumvent the issue by stabilizing the interface and avoiding excessive side reactions.

Conclusions

In summary, we disclose here the fast corrosion of Li on a Cu surface during ageing, which occurs through continuous Kirkendall-type voiding, and the corroded Li can be vulnerable to dendrite

formation in subsequent deposition. Importantly, the fast Li corrosion mainly undergoes a galvanic process, in which Li is oxidized and the electrons are transported through Cu to reduce the electrolyte species. From a careful analysis of the SEIs on Cu and Li, we believe the intrinsically slower electrolyte reduction kinetics on Cu and the resulting porous, organic-rich SEI is the cause of the fast galvanic corrosion. The findings point out a critical issue of Li anodes and offer important supplements to the conventional understanding of corrosion in batteries. This work provides vital insights into the corrosion mechanisms and the corresponding anti-corrosion technology needed to pave the way for future practical Li metal batteries.

Methods

Electrochemistry. Without further specification, the electrochemical cells in the morphological and Coulombic loss studies were demonstrated with 2032-type coin cells. The cells were assembled in an Ar-filled glove box with an O_2 level < 0.2 ppm and a H_2O level <0.1 ppm. High-purity Li foil (750 μm, 99.9% (Alfa Aesar)) and Cu foil (25 μm, 99.8% metal basis (Alfa Aesar)) were employed in all the experiments. Cu foils were first punched into round disks of 2.0 cm², and then washed sequentially with 2-propanol × 1 (Fisher Scientific), 5% HNO_3 × 1 (Sigma-Aldrich), 2-propanol × 1 (Fisher Scientific) and acetone × 2 (Fisher Scientific) to remove the surface oxidants and organic contaminants. Before their transfer, the washed Cu foils were directly dried in the vacuum transfer chamber of the glove box to avoid potential air exposure. If no further specification was required, the electrolyte employed was 1 M LiTFSI (Solvay) in 1:1 w/w DOL/1,2-dimethoxyethane (both Sigma) with 2% $LiNO_3$ (Alfa Aesar). Li foil was punched into 1 cm² round disks and polished thoroughly before the electrochemical tests. Celgard 2325 (25 μm polypropylene–polyethylene–polypropylene) was used as the separator. Galvanostatic charge/discharge was conducted on a LAND 8-channel battery tester, but other electrochemical tests were performed on a Biologic VMP3 system. The electrochemical tests were performed in an environmental chamber (BTU-133, ESPEC North America) at 303 K, which is similar to practical battery operation conditions. The corrosion processes were characterized after resting the Li deposits in the electrolyte for various lengths of time. Note that for the ex situ characterizations (SEM/FIB and cryogenic transmission electron microscope (cryo-TEM)) with '0 hours' of rest, 3–5 min was allowed for specimen preparation, which included cell disassembly, specimen loading and/or transferring.

ALD of LiF. ALD of LiF was performed using a Savannah S100 ALD system (Cambridge NanoTech). The deposition consists of an alternating pulse and purge of LiO^{t}Bu (97% (Sigma-Aldrich)) and TiF_4 (Sigma-Aldrich) as precursors. TiF_4 was gently ground in an Ar glove box before use. Typical pulse and purge durations for the LiO^{t}Bu subcycle were 1 and 25 s, respectively. Typical pulse and purge durations for the TiF_4 subcycle were 0.1 and 25 s, respectively. LiO^{t}Bu was heated to 160–170 °C, and TiF_4 was kept at 115–125 °C. High-purity Ar was used as the carrier gas and the purging gas. LiF thin films were obtained at a deposition temperature of 250 °C.

Material characterization. Either an FEI Strata 235DB dual-beam FIB/SEM or an FEI Helios NanoLab 600i DualBeam FIB/SEM was used for the milling and imaging of the Li deposits. Ga^+ was used as the ion source. Each specimen was washed with 1 ml of DOL in an Ar-filled glove box with an O_2 level < 0.2 ppm and a H_2O level <0.1 ppm to remove the Li salts. A transfer vessel was employed to move the specimens directly from the glove box to the FIB systems to minimize air exposure. Void ratio analyses of the FIB results were performed by image segmentation using ImageJ, in which the void ratio was calculated by the integration of the void area in each slice along the milling progress direction. The XPS characterizations were performed on a PHI Versaprobe I with a monochromatized Al Kα X-ray source. The chamber was kept at a pressure of ~10^{-7} Pa during the characterizations. Each specimen was washed with 1 ml of DOL in an Ar-filled glove box with an O_2 level <0.2 ppm and a H_2O level < 0.1 ppm to remove the Li salts prior to the characterization. A vacuum transfer vessel was used to move the specimens directly into the vacuum transfer chamber of the system to prevent direct air exposure. Ar ion sputtering was employed for the depth profile analysis. A gentle sputtering with a power of 1 kV × 0.5 mA on a 2 mm × 2 mm surface was employed, with the sputtering rate on SiO_2 calibrated to be 2 nm min⁻¹. For the cryo-TEM characterizations, Li was deposited directly on the Cu grid (without carbon). Cells were disassembled in an Ar-filled glove box with an O_2 level <0.2 ppm and a H_2O level < 0.1 ppm. The grids with Li deposits were washed with DOL to remove the Li salts. Once dry, the TEM grid with plated Li was placed in a Teflon-sealed Eppendorf tube and transferred out into the ambient air. The pressure inside the Ar-filled glove box (and thus the Eppendorf tube) is greater than the ambient pressure, which prevents the potential for air to leak into the tube. The sealed Eppendorf tube (with an Ar environment inside) was plunged directly into a bath of liquid nitrogen. We then quickly crushed this

airtight container with a bolt cutter while it was still immersed in liquid nitrogen to rapidly expose the Li metal to the cryogen. The TEM grid was then carefully mounted onto a TEM cryoholder (Gatan) using a cryotransfer station to ensure the entire process occurred under liquid nitrogen. During insertion into the TEM column (~1 s), a built-in shutter on the holder was closed to prevent contact of metallic Li with the air. In this way, the reactive battery material can be safely transferred from a cell to the TEM without any chance of ambient air exposure. Once inside the TEM column, the sample was kept cold at −178 °C. The TEM characterizations were then carried out using a FEI Titan 80-300 environmental (scanning) transmission electron microscope operated at 300 kV. The microscope was equipped with an aberration corrector in the image-forming (objective) lens, which was tuned before each sample analysis. Other non-destructive SEM images were taken with a FEI XL30 Sirion scanning electron microscope system. The cells were disassembled in an Ar-filled glove box with an O_2 level <0.2 ppm and a H_2O level <0.1 ppm. Each specimen was washed with 1 ml of DOL in an Ar-filled glove box with an O_2 level <0.2 ppm and a H_2O level <0.1 ppm to remove the Li salts. A transfer vessel was employed to move the specimens directly from the glove box to the SEM system to minimize air exposure. X-ray diffraction was measured on a Bruker D8 Venture with a Cu Kα source. ImageJ was used to process the statistic analysis of Li particle size distribution.

Data availability
All the data supporting the findings of this study are available within the article and its Supplementary Information, and from the corresponding authors upon reasonable request.

References
1. Jones, D. A. *Principles and Prevention of Corrosion* (Macmillan, New York, 1992).
2. Bard, A. J., Faulkner, L. R., Leddy, J. & Zoski, C. G. *Electrochemical Methods: Fundamentals and Applications* Vol. 2 (Wiley, New York, 1980).
3. Winter, M. & Brodd, R. J. What are batteries, fuel cells, and supercapacitors? *Chem. Rev.* **104**, 4245–4270 (2004).
4. Tarascon, J.-M. & Armand, M. Issues and challenges facing rechargeable lithium batteries. *Nature* **414**, 359–367 (2001).
5. Goodenough, J. B. & Park, K.-S. The Li-ion rechargeable battery: a perspective. *J. Am. Chem. Soc.* **135**, 1167–1176 (2013).
6. Park, H. et al. Thermal behavior of solid electrolyte interphase films deposited on graphite electrodes with different states-of-charge. *J. Electrochem. Soc.* **162**, A892–A896 (2015).
7. Fong, R., von Sacken, U. & Dahn, J. R. Studies of lithium intercalation into carbons using nonaqueous electrochemical cells. *J. Electrochem. Soc.* **137**, 2009–2013 (1990).
8. Dunn, B., Kamath, H. & Tarascon, J.–M. Electrical energy storage for the grid: a battery of choices. *Science* **334**, 928–935 (2011).
9. Bruce, P. G., Freunberger, S. A., Hardwick, L. J. & Tarascon, J.-M. Li–O_2 and Li–S batteries with high energy storage. *Nat. Mater.* **11**, 19–29 (2012).
10. Aurbach, D. et al. On the surface chemical aspects of very high energy density, rechargeable Li–sulfur batteries. *J. Electrochem. Soc.* **156**, A694–A702 (2009).
11. Harrison, K. L. et al. Lithium self-discharge and its prevention: direct visualization through in situ electrochemical scanning transmission electron microscopy. *ACS Nano* **11**, 11194–11205 (2017).
12. Pei, A., Zheng, G., Shi, F., Li, Y. & Cui, Y. Nanoscale nucleation and growth of electrodeposited lithium metal. *Nano Lett.* **17**, 1132–1139 (2017).
13. Yang, H., Fey, E. O., Trimm, B. D., Dimitrov, N. & Whittingham, M. S. Effects of pulse plating on lithium electrodeposition, morphology and cycling efficiency. *J. Power Sources* **272**, 900–908 (2014).
14. Zheng, J. et al. Electrolyte additive enabled fast charging and stable cycling lithium metal batteries. *Nat. Energy* **2**, 17012 (2017).
15. Chen, S. et al. High-efficiency lithium metal batteries with fire-retardant electrolytes. *Joule* **2**, 1548–1558 (2018).
16. Fan, X. et al. Non-flammable electrolyte enables Li–metal batteries with aggressive cathode chemistries. *Nat. Nanotech.* **13**, 715–722 (2018).
17. Kozen, A. C. et al. Next-generation lithium metal anode engineering via atomic layer deposition. *ACS Nano* **9**, 5884–5892 (2015).
18. Liu, Y. et al. An ultrastrong double-layer nanodiamond interface for stable lithium metal anodes. *Joule* **2**, 1595–1609 (2018).
19. Xie, J. et al. Stitching h-BN by atomic layer deposition of LiF as a stable interface for lithium metal anode. *Sci. Adv.* **3**, eaao3170 (2017).
20. Lin, D. et al. Layered reduced graphene oxide with nanoscale interlayer gaps as a stable host for lithium metal anodes. *Nat. Nanotech.* **11**, 626–632 (2016).
21. Yang, C.-P., Yin, Y.-X., Zhang, S.-F., Li, N.-W. & Guo, Y.-G. Accommodating lithium into 3D current collectors with a submicron skeleton towards long-life lithium metal anodes. *Nat. Commun.* **6**, 8058 (2015).
22. Xu, W. et al. Lithium metal anodes for rechargeable batteries. *Energy Environ. Sci.* **7**, 513–537 (2014).
23. Lin, D., Liu, Y. & Cui, Y. Reviving the lithium metal anode for high-energy batteries. *Nat. Nanotech.* **12**, 194–206 (2017).
24. Qian, J. et al. High rate and stable cycling of lithium metal anode. *Nat. Commun.* **6**, 6362 (2015).
25. Ryou, M. H., Lee, Y. M., Lee, Y., Winter, M. & Bieker, P. Mechanical surface modification of lithium metal: towards improved Li metal anode performance by directed Li plating. *Adv. Funct. Mater.* **25**, 834–841 (2015).
26. Peled, E. The electrochemical behavior of alkali and alkaline earth metals in nonaqueous battery systems—the solid electrolyte interphase model. *J. Electrochem. Soc.* **126**, 2047–2051 (1979).
27. Aurbach, D., Gofer, Y. & Langzam, J. The correlation between surface chemistry, surface morphology, and cycling efficiency of lithium electrodes in a few polar aprotic systems. *J. Electrochem. Soc.* **136**, 3198–3205 (1989).
28. Aurbach, D., Youngman, O. & Dan, P. The electrochemical behavior of 1, 3-dioxolane–$LiClO_4$ solutions—II. Contaminated solutions. *Electrochim. Acta* **35**, 639–655 (1990).
29. Odziemkowski, M. & Irish, D. E. An electrochemical study of the reactivity at the lithium electrolyte/bare lithium metal interface: I. Purified electrolytes. *J. Electrochem. Soc.* **139**, 3063–3074 (1992).
30. Aurbach, D., Ein-Ely, Y. & Zaban, A. The surface chemistry of lithium electrodes in alkyl carbonate solutions. *J. Electrochem. Soc.* **141**, L1–L3 (1994).
31. Peled, E., Golodnitsky, D. & Ardel, G. Advanced model for solid electrolyte interphase electrodes in liquid and polymer electrolytes. *J. Electrochem. Soc.* **144**, L208–L210 (1997).
32. Aurbach, D., Zinigrad, E., Cohen, Y. & Teller, H. A short review of failure mechanisms of lithium metal and lithiated graphite anodes in liquid electrolyte solutions. *Solid State Ionics* **148**, 405–416 (2002).
33. Aurbach, D. Review of selected electrode–solution interactions which determine the performance of Li and Li ion batteries. *J. Power Sources* **89**, 206–218 (2000).
34. Cheng, X. B. et al. A review of solid electrolyte interphases on lithium metal anode. *Adv. Sci.* **3**, 1500213 (2016).
35. Keil, P. et al. Calendar aging of lithium-ion batteries: I. Impact of the graphite anode on capacity fade. *J. Electrochem. Soc.* **163**, A1872–A1880 (2016).
36. Smigelskas, A. & Kirkendall, E. Zinc diffusion in alpha brass. *Trans. Metall. Soc. AIME* **171**, 130–142 (1947).
37. Yin, Y. et al. Formation of hollow nanocrystals through the nanoscale Kirkendall effect. *Science* **304**, 711–714 (2004).
38. Chee, S. W., Tan, S. F., Baraissov, Z., Bosman, M. & Mirsaidov, U. Direct observation of the nanoscale Kirkendall effect during galvanic replacement reactions. *Nat. Commun.* **8**, 1224 (2017).
39. Oldfield, J. W. in *Galvanic Corrosion* (ed. Hack, H. P.) 5–22 (ASTM International, Philadelphia, 1988).
40. Li, W. et al. The synergetic effect of lithium polysulfide and lithium nitrate to prevent lithium dendrite growth. *Nat. Commun.* **6**, 7436 (2015).
41. Li, Y. et al. Atomic structure of sensitive battery materials and interfaces revealed by cryo-electron microscopy. *Science* **358**, 506–510 (2017).
42. Peled, E. & Menkin, S. SEI: past, present and future. *J. Electrochem. Soc.* **164**, A1703–A1719 (2017).
43. Chen, K. -H. et al. Dead lithium: mass transport effects on voltage, capacity, and failure of lithium metal anodes. *J. Mater. Chem. A* **5**, 11671–11681 (2017).
44. Soto, F. A., Ma, Y., Martinez de la Hoz, J. M., Seminario, J. M. & Balbuena, P. B. Formation and growth mechanisms of solid–electrolyte interphase layers in rechargeable batteries. *Chem. Mater.* **27**, 7990–8000 (2015).
45. Anderson, B. D. & Tracy, J. B. Nanoparticle conversion chemistry: Kirkendall effect, galvanic exchange, and anion exchange. *Nanoscale* **6**, 12195–12216 (2014).
46. Xu, K. Nonaqueous liquid electrolytes for lithium-based rechargeable batteries. *Chem. Rev.* **104**, 4303–4418 (2004).
47. Xu, K. Electrolytes and interphases in Li-ion batteries and beyond. *Chem. Rev.* **114**, 11503–11618 (2014).
48. Thevenin, J. & Muller, R. Impedance of lithium electrodes in a propylene carbonate electrolyte. *J. Electrochem. Soc.* **134**, 273–280 (1987).
49. Peled, E. et al. The role of SEI in lithium and lithium ion batteries. *Mater. Res. Soc. Symp.* **393**, 209 (1995).

Author contributions
D.L., Y.Liu and Y.C. conceived the project and designed the experiments. D.L. and Y.Liu performed the electrochemical studies. D.L. and Y.Liu conducted the FIB

Competing interests

The authors declare no competing interests.

Additional information

Supplementary information is available for this paper at https://doi.org/10.1038/s41557-018-0203-8.

Reprints and permissions information is available at www.nature.com/reprints.

Correspondence and requests for materials should be addressed to Y.C.

Publisher's note: Springer Nature remains neutral with regard to jurisdictional claims in published maps and institutional affiliations.